AIP | Journal of Applied Physics

Mass correlation spectroscopy for mass- and size-based nanoparticle characterization in fluid

Mario M. Modena and Thomas P. Burg

Citation: Journal of Applied Physics **118**, 224901 (2015); doi: 10.1063/1.4937151
View online: http://dx.doi.org/10.1063/1.4937151
View Table of Contents: http://scitation.aip.org/content/aip/journal/jap/118/22?ver=pdfcov
Published by the AIP Publishing

Mass correlation spectroscopy for mass- and size-based nanoparticle characterization in fluid

Mario M. Modena and Thomas P. Burg[a)]
Max Planck Institute for Biophysical Chemistry, Göttingen, Germany

(Received 19 August 2015; accepted 22 November 2015; published online 8 December 2015)

The characterization of nanoparticles is an important problem in many areas of applied physics, chemistry, medicine, and biology. Micromechanical resonators with embedded fluidic channels represent a powerful new technology for particle characterization through direct measurement of the buoyant mass of nanoparticles in solution with attogram resolution (1 ag = 10^{-18} g). We recently showed that correlation analysis greatly expands the range of applications by enabling measurements of mass even when the individual particles are far lighter than the conventional detection limit. Here, we extend the concept of mass correlation spectroscopy further to simultaneously measure the ensemble-averaged size and mass of nanoparticles by exploiting size-dependent differences in hydrodynamic dispersion. To do so, we first derive an approximate model of the dispersion of finite-size particles flowing through a microfluidic channel of rectangular cross-section, valid in a large range of dispersion regimes. By including this solution into the model describing the correlation function of the time-domain mass signal acquired with a micromechanical resonator, information on particle size can be obtained during mass characterization without requiring any modification of the devices. The validity of the analysis is corroborated both by numerical simulations and experimental measurements on nanoparticles of different materials ranging from 15 nm to 500 nm. [http://dx.doi.org/10.1063/1.4937151]

I. INTRODUCTION

Understanding the composition and the behavior of nanoparticles has required the development of a large variety of techniques[1–8] to detect their chemical and physical properties, as well as their interactions with the environment. Dynamic light scattering[1] (DLS) is maybe the most widely used detection method for the sizing of particles in solution, thanks to the low sample volume requirement (∼10 μl), wide dynamic range (from nanometer to micrometer size), and ease of operation.[5] The main drawbacks of the analysis are the limitation to optically clear samples and, most importantly, the low resolving power when dealing with heterogeneous populations of particles. High precision characterization of particles in solution can be obtained by analytical centrifugation, which also allows population separation and deconvolution during the analysis.[3] However, the high costs of the equipment and the relatively long analysis times hinder the routine application of this method. Another class of analysis method is represented by high-resolution microscopy techniques, such as electron microscopy[9] or atomic force microscopy,[10] which enable visual inspection of the sample. Information on the size and shape of the objects under examination can be obtained with nanometer resolution. However, these methods are characterized by low-throughput and potential image artifacts, caused by the extensive sample preparation required.[5,8]

Recently, micromechanical resonators have been proven as an extraordinary tool for mass characterization,[11–13] reaching sub-atomic resolution for samples in vacuum.[14,15] For liquid samples, the embedding of a microfluidic channel in the resonating structure has opened the way to the characterization of mass and density of particles in solution.[16–19] The resonators act as mass/frequency transducer, where variations of the effective mass of the resonator, caused by the particles flowing in the embedded channel, can be detected by monitoring the resonance frequency of the device. The magnitude of the induced frequency variation is linearly proportional to the ratio between the mass of the particles and that of the resonator. The miniaturization of the devices to sub-micrometer dimensions has recently allowed the realization of devices with single-particle detection limit of ∼5 ag (1 ag = 10^{-18} g).[20] We have previously demonstrated that mass resolution can be enhanced by over four orders of magnitude by applying a correlation analysis of the time-domain mass signal.[21] By developing an approximate model for the autocorrelation function, information on the mass and concentration of the particles could be retrieved by the interpretation of the magnitude of the correlation curve. Although we have shown that the curve shape contains information on the particle size, the lack of a model describing the diffusion/dispersion behavior of the particles while crossing the embedded microfluidic channel prevented the extraction of such information.

We present here an approximate solution of the axial dispersion of finite-size particles subjected to a pressure-driven laminar flow in a microfluidic channel of rectangular cross-section. By integrating this model into the description of the correlation analysis of the mass signal recorded by embedded channel resonators, information on particle size can be extracted during mass characterization.

As cantilever resonators with embedded microfluidic channels, the so-called suspended microchannel resonators (SMRs), represent the most widely used class of resonator devices,[16,19,20] the correlation analysis presented here will focus on the signal obtained with cantilever structures vibrating in the first resonant mode. Nevertheless, these results can be applied to any type of resonators by substituting the appropriate sensitivity profile in the following analysis.

[a)]Electronic mail: tburg@mpibpc.mpg.de

II. THEORY

Particles flowing through the microfluidic channel embedded in the resonator induce a position dependent shift in the resonance frequency of the device, given by[22]

$$\delta f_p(x) = u(x)^2 f_{p0}, \tag{1}$$

where $u(x)$ is the normalized deflection function of the resonator. The frequency shift f_{p0} induced when a particle passes the point of maximum deflection is given by[16]

$$f_{p0} = -\frac{1}{2}\frac{\Delta m_p}{m^*} f_0, \tag{2}$$

where m^* is the effective mass of the resonator, f_0 is the resonance frequency of the device filled with solution, and $\Delta m_p = m_p \cdot (1 - \rho_b/\rho_p)$ denotes the buoyant mass of the particle. Here, m_p is the dry mass of the particle, while ρ_b and ρ_p are the densities of the buffer and the particle, respectively. When the sample concentration is such that more than one particle is in the channel at any moment, the effective mass density of the fluid is altered and the resonator presents a static shift in resonance frequency, proportional to the solid content of the solution. This shift is usually too small to be quantified with precision, as slow varying noise terms, such as mechanical and thermal drifts or fluctuations in supply pressure, might easily overcome this effect. On the contrary, frequency fluctuations induced by particle number variations can be used to separate the particle and noise contributions in the signal, enabling mass characterization of particles in solution even when the individual particle signatures cannot be detected.[21] This resolution enhancement is achieved by using a correlation analysis of the time-domain mass signal. This type of analysis will be here referred to as Mass Correlation Spectroscopy (MCS).

Assuming a sample of identical particles, the fluctuations of the resonance frequency are described by

$$\delta f(t) = f_{p0} \cdot \int_V \delta c(x,y,z,t) \cdot u(x)^2 \mathrm{d}y\mathrm{d}z\mathrm{d}x, \tag{3}$$

where the integral is calculated over the volume V of the embedded microfluidic channel and $\delta c(x,y,z,t)$ denotes the concentration fluctuation at position (x, y, z). $\delta f(t)$ only describes the frequency fluctuations around the average resonance value and experimentally corresponds to the high-pass filtered signal, with zero mean and no baseline drift. The autocorrelation of the frequency fluctuation is defined as

$$C(\tau) = \langle \delta f(t) \delta f(t+\tau) \rangle, \tag{4}$$

where "$\langle \bullet \rangle$" is the ensemble-based expected value.[23] By inserting Eq. (3) in Eq. (4) and assuming that the correlation only depends on the time difference τ, the autocorrelation is calculated as

$$\begin{aligned} C(\tau) = & f_{p0}^2 \int\int_V \langle \delta c(x,y,z,0) \delta c(x',y',z',\tau) \rangle \\ & \times u(x)^2 u(x')^2 \mathrm{d}y\mathrm{d}z\mathrm{d}x\mathrm{d}y'\mathrm{d}z'\mathrm{d}x'. \end{aligned} \tag{5}$$

Using a linear approximation of the cantilever deflection in the first resonant mode, the amplitude at lag zero of the correlation function can be readily calculated and corresponds to[21]

$$C(0) = \frac{1}{5} f_{p0}^2 c_0 V, \tag{6}$$

where c_0 is the particle concentration and the numerical factor 1/5 depends on the sensitivity profile of the resonator. For a sample of non-identical particles, f_{p0}^2 should be substituted by $\langle f_{p0}^2 \rangle$. From Eq. (6), it can be noticed that the correlation amplitude provides information on the buoyant mass of the particles in solution and on their concentration. Assuming a white noise with variance σ_n^2 during acquisition, the residual noise around lag zero in the correlation curve has variance $\sigma_{\hat{C}}^2 \approx \sigma_n^4/N$, where N defines the number of points of the experimental trace, and $\hat{C}$ indicates the experimental autocorrelation curve. The signal-to-noise ratio (S/N) of the correlation curve is given by[21]

$$\mathrm{S/N} \geq \frac{1}{5}\frac{f_{p0}^2}{\sigma_n^2} c_0 V \sqrt{T_{meas} f_s}, \tag{7}$$

where $N = T_{meas} \cdot f_s$, T_{meas} denotes the acquisition time, and f_s the sampling frequency. Eq. (7) indicates that the detection limit of mass measurements by MCS is ultimately defined by the acquisition time, hence by the sample volume and flow stability, and by the particle concentration.

In the following, we explore the possibility of measuring particle size rather than mass through a detailed analysis of the shape of the autocorrelation curve. The effects of diffusion and finite-particle size are shown qualitatively in Fig. 1. The temporal evolution of the concentration fluctuations is described by the convection-diffusion equation

$$\frac{\partial \delta c}{\partial t} = D\left[\frac{\partial^2 \delta c}{\partial x^2} + \frac{\partial^2 \delta c}{\partial y^2} + \frac{\partial^2 \delta c}{\partial z^2}\right] - U(y,z)\frac{\partial \delta c}{\partial x}, \tag{8}$$

where D is the diffusion coefficient of the particles, and $U(y, z)$ is the velocity profile described by[24]

$$U(y,z) = U_{max}\left[1 - \frac{y^2}{h^2} - \frac{32}{\pi^3}\sum_{n=0}^{\infty}\frac{(-1)^n}{(2n+1)^3} \times \frac{\cosh\left(\frac{(2n+1)\pi y}{2h}\right)}{\cosh\left(\frac{(2n+1)\pi}{2\beta}\right)}\cos\left(\frac{(2n+1)\pi z}{2h}\right)\right], \tag{9}$$

with $U_{max} = U(0,0)$ the maximum flow velocity at the center of the cross-section, and $\beta = h/b$ the channel aspect ratio. The initial and boundary conditions are

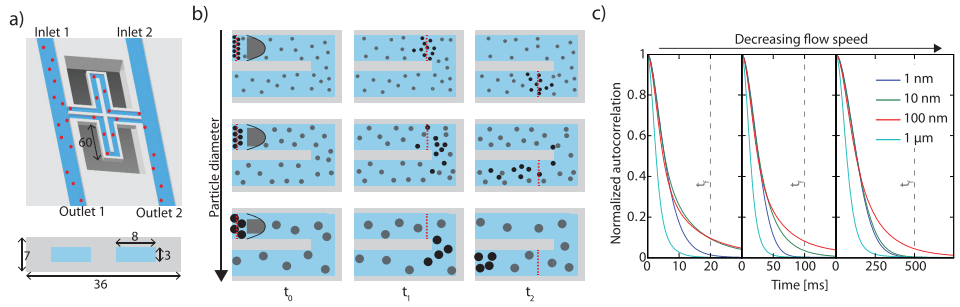

FIG. 1. (a) Schematic representation of the torsional SMR used for the particle characterization. Each paddle measures 60 μm and contains a rectangular embedded microfluidic channel of cross-section $3 \times 8\ \mu m^2$. Pressurized inlets and outlets allow rapid changes of the solutions and fine control of the flow velocity in the resonator; (b) axial dispersion of a plug of particles subjected to laminar flow. The gray shaded areas highlight the velocity profile accessible to particles of different sizes in the channel. The dashed (red) lines indicate the average distance traveled by the fluid at time t. Small particles present a very narrow axial distribution as the rapid diffusion of the particles in the cross-section quickly smoothes out velocity differences between particles. The plug of particles travels at the average fluid velocity, since particles can closely approach the walls. Larger particles are excluded from the slowest regions of the profile and present a larger axial distribution, because of the low averaging effect of diffusion. However, particles of size comparable to the cross section dimensions (bottom sketch) are only subjected to the central part of the velocity profile, hence experiencing a very narrow velocity distribution. The plug moves at an average velocity much higher than the fluid; (c) expected mass correlation signals for particles of various sizes subjected to different flow velocities and flowing in the channel depicted in Fig. 1(a). The axial dispersion of the 1 nm and 1 μm particles has a low dependence on flow velocity; therefore, the autocorrelation shape is similar for the three cases. Particles, whose size falls between these two extremes, present a flow dependent autocorrelation shape, according to the average radial diffusion of the particles. The variation of autocorrelation shape with particle size is a function of flow velocities and channel dimensions.

$$\delta c(x,y,z,0) = \delta(x)\Phi(y,z), \tag{10a}$$

$$\left.\frac{\partial \delta c}{\partial y}\right|_{y=-b,b} = 0, \tag{10b}$$

$$\left.\frac{\partial \delta c}{\partial z}\right|_{z=-h,h} = 0, \tag{10c}$$

$$\lim_{x\to\infty} c = \lim_{x\to\infty} \frac{\partial \delta c}{\partial x} = 0. \tag{10d}$$

The conventions used for the calculations are shown in Fig. 2. Since fluctuations have uniform probability of being generated anywhere in the channel, $\Phi(y,z) = c_0$ (for $|y| < (b - r_p)$ and $|z| < (h - r_p)$, with r_p the particle radius) corresponds to a uniform particle distribution over the cross-section.

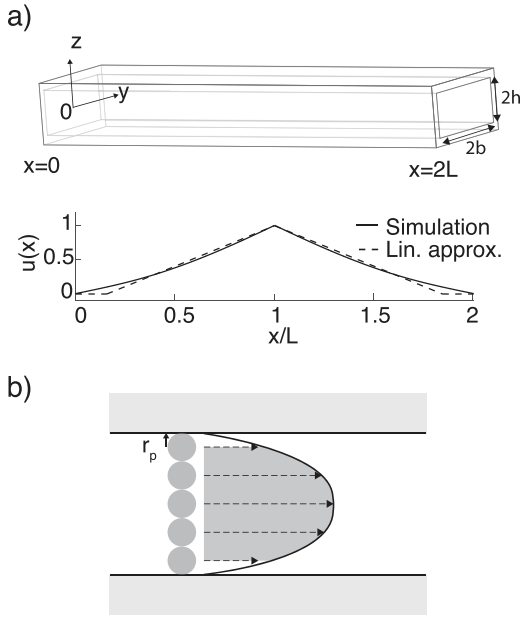

FIG. 2. (a) The embedded microfluidic channel is mapped to a linear geometry of length $2L$ and cross-section dimensions $2b \times 2h$. Inertial effects caused by the channel curvature are neglected as the Reynolds number is Re ≈ 0.01. The lower graph shows the comparison between the expected deflection function $u(x)$ and the linear approximation used for the calculations; (b) particles of finite size cannot approach the walls and are excluded from the slowest regions of the velocity profile.

Following the procedure of Doshi *et al.*,[24] it is convenient to construct a solution for the concentration fluctuations integrated over the cross-section

$$\delta c_m(x,t) = \int_{-b}^{b}\int_{-h}^{h} \delta c(x,y,z,t)\mathrm{d}y\mathrm{d}z. \tag{11}$$

Inserting Eq. (11) in Eq. (5), the autocorrelation function can be rewritten as

$$C(\tau) = f_{p0}^2 \int\int_0^{2L} \langle \delta c_m(x,0)\delta c_m(x',\tau)\rangle \times u(x)^2 u(x')^2 \mathrm{d}x\mathrm{d}x'. \tag{12}$$

Although there is no complete analytical solution for the problem described in Eqs. (8) and (10), approximate solutions for $\delta c_m(x,t)$ valid for different regimes can be constructed. In the literature, the special case of point-like particles in channels of circular cross-sections has been discussed extensively.[25] However, this situation is seldom encountered in microfluidics, as rectangular cross-sections are more easily obtained by micro-fabrication techniques and particle size can be comparable to the channel dimensions. We derive here an approximate solution for $\delta c_m(x,t)$ that covers the entire range of experimental conditions relevant for correlation measurements in micrometer and submicrometer fluidic channels.

Different dispersion regimes in the axial direction can be identified according to the extension of particle diffusion in the cross-section. A dimensionless time parameter

$$\tau_D = \frac{D\,t}{a^2}, \tag{13}$$

can be defined to quantify the average radial diffusion of the particles. Here, t is the dimensional time, and a is the

characteristic channel dimension (e.g. the channel radius or, for high aspect ratio rectangular channels, the minimum cross-section dimension). For $\tau_D \ll 1$, particles do not diffuse considerably and follow their streamline. This situation will be defined as "advection regime". For $\tau_D > 1$, particles have sampled, on average, the entire flow profile. As this regime was first investigated by Taylor for channels of circular cross-section,[26] it is referred to as "Taylor regime." The third case, for $0 < \tau_D < 1$, corresponds to the transition from the advection to the diffusion dominated dispersion regimes.

Once the particle behavior for $\tau_D \ll 1$ and $\tau_D > 1$ is known, the concentration profile at any time can be interpolated by a weighted sum of the limiting cases[27] as

$$\delta c_m(x,t) = A(t) \cdot \delta c_{mA}(x,t) + (1 - A(t)) \cdot \delta c_{mT}(x,t), \quad (14)$$

where $\delta c_{mA}(x,t)$ and $\delta c_{mT}(x,t)$ denote the axial profile of the concentration fluctuation in the advection and Taylor regime, respectively, and $A(t)$ is a time-dependent amplitude factor. In the derivation of the approximate model, particles are assumed to be moving at the fluid velocity of their center of mass and that their presence does not affect the flow profile in the cross-section. An interesting effect not included in this model is that there is a possibility for particles to cross streamlines of the fluid due to the acceleration of the vibrating resonator. For the experimental conditions considered in this work, this displacement can be estimated to be on the 10 nm scale and can be safely neglected. However, by increasing the vibration amplitude and the vibration frequency, for example when using higher order modes, the phenomenon could in principle be amplified to a measurable level.

A. Taylor regime

This regime occurs when the average diffusion length of the particles exceeds the characteristic dimension of the cross-section, i.e., for $\tau_D > 1$. As shown by Taylor[26] and Aris[28] for round cross-section channels, a plug of sample reaches a Gaussian distribution in the axial direction, regardless of the original radial distribution.[28] It was later demonstrated that this solution applies to channels of arbitrary cross-section, with channel geometry influencing the variance of the axial distribution of the particles.[29]

For point-like particles flowing in a rectangular channel, a solution for $\delta c_{mT}(x,t)$ was derived by Doshi *et al.*,[24] corresponding to

$$\delta c_{mT}(x,t) = c_0 V \frac{\exp\left[-\frac{(x - U_{avg}t)^2}{4\bar{k}(t)t}\right]}{\sqrt{4\pi\bar{k}(t)t}}. \quad (15)$$

The profile follows a Gaussian distribution moving at the average flow velocity U_{avg}. The parameter $\bar{k}(t)$ is defined as

$$\bar{k}(t) = \frac{1}{t}\int_0^t k(t')\mathrm{d}t', \quad (16)$$

with

$$k(t) = D\left[1 + \left(\frac{U_{max}h}{D}\right)^2 (K_{horiz}(t) + K_{vert}(t))\right], \quad (17)$$

containing information on the particle diffusivity D, the flow velocity, and the channel dimensions. The horizontal and vertical dispersion parameters are defined as

$$K_{horiz}(t) = \sum_{m=1}^{\infty} B_m^2\left(1 - \exp\left[-\frac{m^2\pi^2 tD}{b^2}\right]\right), \quad (18a)$$

$$K_{vert}(t) = \sum_{n=1}^{\infty} B_n^2\left(1 - \exp\left[-\frac{n^2\pi^2 tD}{h^2}\right]\right), \quad (18b)$$

with

$$B_m = \frac{256(-1)^m}{\pi^6 m}\sum_{j=1,3,5}^{\infty}\frac{\tanh\left(\frac{j\pi}{2\beta}\right)}{j^3\left[j^2 + 4m^2\beta^2\right]}, \quad (19a)$$

$$B_n = \frac{4(-1)^n}{\pi^3 n^3} + \frac{256(-1)^{n+1}\beta}{\pi^6 n} \times \sum_{j=1,3,5}^{\infty}\frac{\tanh\left(\frac{j\pi}{2\beta}\right)}{j^3(2n+j)(2n-j)}. \quad (19b)$$

Particles of finite size are excluded from the slowest regions of the velocity profile, and therefore experience a narrower velocity distribution. This affects both the average velocity of the particles and their dispersion.[30] Defining the particle radius r_p, the effective average velocity can be calculated as

$$U_{eff} = \frac{1}{b'}\frac{1}{h'}\int_0^{b'}\int_0^{h'} U(y,z)\mathrm{d}z\mathrm{d}y, \quad (20)$$

where $h' = h - r_p$ and $b' = b - r_p$ are the effective dimensions of the channel. From Eq. (20), it follows that particles of finite size, on average, move faster than the suspending fluid. Following this result, the average velocity in Eq. (15) has to be substituted by U_{eff} of Eq. (20) when dealing with particles of non-negligible size. Despite the simplicity of the calculation of U_{eff}, this solution approximates well the behavior of particles of size comparable to the channel dimensions, as shown later by the validation measurements.

Finally, excluding particles from the slowest regions of the velocity profile causes a reduction in the sample dispersion coefficient, as particles are subjected to a narrower velocity distribution. Following the results of James and Chrysikopoulos for particles flowing in parallel plate conduits,[30] the dispersion coefficient $k(t)$ for particles of finite size is calculated by modifying the horizontal and vertical contributions as

$$K'_{horiz}(t) = \sum_{m=1}^{\infty} B_m^2\left(1 - \exp\left[-\frac{m^2\pi^2 tD}{b'^2}\right]\right) \cdot \left(1 - \frac{r_p}{b}\right)^6, \quad (21a)$$

$$K'_{vert}(t) = \sum_{n=1}^{\infty} B_n^2\left(1 - \exp\left[-\frac{n^2\pi^2 tD}{h'^2}\right]\right) \cdot \left(1 - \frac{r_p}{h}\right)^6. \quad (21b)$$

B. Advection regime

For $\tau_D \ll 1$, particles can only diffuse by a small fraction of the channel during their passage through the mass sensor. To describe this situation, we divided the cross-section into M compartments. In each compartment, the velocity profile is approximated with a linear function. As a consequence, the dispersion in each compartment can be calculated with the formula for a plane Couette flow, defined as[31]

$$k_{Ai} = D\left[1 + \frac{1}{30}Pe_i^2\right], \tag{22}$$

where $Pe_i = \Delta U_i w/D$ is the Péclet number in the compartment i. Since dispersion is caused by velocity differences between particles, ΔU_i represents the velocity variation with respect to the average speed U_i in the i-th compartment. w is the compartment size, defined as $w = \sqrt{4bh/M}$. With this approximation, the axial concentration profile can be expressed by a mathematical description similar to the solution found for $\tau_D > 1$. Here

$$\delta c_{mA}(x,t) = \frac{c_0 V}{M}\sum_{i=1}^{M}\frac{\exp\left[-\dfrac{(x-U_i t)^2}{4k_{Ai}t}\right]}{\sqrt{4\pi k_{Ai}t}}. \tag{23}$$

To account for the finite size of the particles, it is sufficient to apply the compartmentalization over the regions accessible to the particles, i.e.,

$$-b' \le y \le b', \tag{24a}$$

$$-h' \le z \le h', \tag{24b}$$

where b' and h' are the effective channel dimensions, as defined before.

C. Concentration dispersion model

The transition from the advection to the Taylor regime presents a dependence both on particle diffusion and channel aspect-ratio. Defining

$$A_h(t) = \frac{1-\exp\left[-9Dt/b'^2\right]}{9Dt/b'^2}, \tag{25a}$$

$$A_v(t) = \frac{1-\exp\left[-9Dt/h'^2\right]}{9Dt/h'^2}, \tag{25b}$$

the dispersion coefficients (Eq. (18)) in the horizontal and vertical dimensions tend to their steady state values as, approximately, $1 - A_h(t)$ and $1 - A_v(t)$, respectively. The factor 9 in the equation derives from the symmetry planes in the velocity distribution for a rectangular cross-section channel.[32] Including a dependence on the channel aspect-ratio, the time-dependent weighing factor $A(t)$ of Eq. (14) can be defined as

$$A(t) = \beta \cdot A_h(t) + (1-\beta)\cdot A_v(t). \tag{26}$$

Inserting Eq. (26), Eq. (23), and Eq. (15) in Eq. (14), it is now possible to describe the evolution of an initially uniformly distributed concentration fluctuation at any time.

III. MATERIALS AND METHODS

A. Suspended microchannel resonators

We used a torsional resonator as sketched in Fig. 1(a). Each paddle measures $60 \times 36 \times 7\ \mu m^3$ (length × width × thickness), and it contains a U-shaped microfluidic channel with cross-section $3 \times 8\ \mu m^2$. The resonator presented a resonance frequency of ~1.17 MHz, quality factor ~23 000 under nitrogen gas flow, and ~1.12 MHz when filled with water, quality factor ~6000. The change in quality factor upon filling with water is expected due to the high operating frequency of the torsional resonator.[33] The same device was used for all experiments. The fabrication of the device has been described previously,[16] and only the key steps are reported here. First, the embedded microfluidic channel is etched into silicon with a nominal depth of 3 μm and sealed by fusion bonding with another silicon wafer. Then, the silicon is dry etched to define the resonator structure. To reduce the viscous damping of the resonator, the device is vacuum packaged by bonding two Pyrex wafers, one of which contains the electrostatic actuation electrode.

To avoid contamination between measurements, the devices were thoroughly rinsed between samples. In case of clogging, a solution of sulfuric acid and hydrogen peroxide (2:1, piranha solution) was used to clear the channels. Background measurements of pure milli-Q water were taken before and after measurements to check that the microfluidic channels had been properly emptied from previous samples. The device was placed on a temperature controlled stage, and all measurements were performed at 25 °C. The noise level during measurement in 1 kHz bandwidth was ~200 mHz and ~400 mHz in a 2 kHz bandwidth. The detection of the resonator oscillation was performed by using an optical lever, whose signal fed a closed-loop feedback circuit where the resonator represents the oscillatory element, followed by an amplitude-controlled gain circuit to ensure linearity in the device oscillation. The resonator is excited electrostatically.[34] Fluid flow was controlled by means of external pressurized inlets and outlets that ensured smooth, pulse-free flow through the resonator. The inlets and outlets of the chip were pressurized to approximately 15 kPa, and a pressure difference of a few kPa was applied between the delivery channels to control the flow in the detection channels.

B. Numerical simulations

A plug of 5000 simulated non-interacting particles released at the entrance of the microfluidic channel was subjected to advection and diffusion. The magnitude of advection per time step was $U(y_i, z_i)\Delta t$, where $U(y_i, z_i)$ corresponded to the flow velocity at the particle position, and Δt the simulation time increment. Particles were free to diffuse in three dimensions, with an average diffusion length of $\sqrt{D\Delta t}$ per time step and in each direction. The time increment Δt was chosen such that particles needed, on average, more than 200 steps to transit through the simulated channel. All Monte Carlo (MC) simulations were performed with a custom MATLAB script.

C. Sample preparation

15 nm gold nanoparticles (Nanopartz, Inc., P/N A11–15) suspended in pure milli-Q water were measured at a concentration of 1.6×10^{12} ml^{-1}; 30 nm gold nanoparticles (Nanopartz Inc, P/N A11-30) were suspended in pure milli-Q water at a concentration of 1.02×10^{11} ml^{-1}; 85 nm polystyrene beads (Polysciences Inc, P/N 16688) and 210 nm polystyrene beads (Invitrogen, P/N F8809) were suspended in an aqueous buffer containing 100 mM NaCl, 350 μm SDS, sodium dodecyl sulfate (SDS) and 0.01% w/v NaN_3 at concentrations of 7.7×10^{12} ml^{-1} and 1.2×10^{11} ml^{-1}, respectively. The purpose of the buffer was to minimize the risk of particle aggregation or interaction with the walls; 490 nm polystyrene beads (Polysciences, Inc., P/N 18720) were suspended in pure milli-Q water at a concentration of 4×10^8 ml^{-1}. Furthermore, a sample composed of a mixture of 93 nm polystyrene nanoparticles (Phosphorex Inc, P/N 105) and 490 nm polystyrene particles was prepared by diluting the stock solutions in pure milli-Q water. The concentrations of the two particle populations were 5.7×10^{12} ml^{-1} and 5.4×10^8 ml^{-1}, respectively. Sample solutions were prepared before each experiment and ultrasonicated for $\sim$1 min to reduce unwanted particle aggregations.

All solutions analyzed with the SMR device were mixed with a small concentration (5×10^6 ml^{-1}) of 1.54 μm NIST polystyrene beads (Polysciences Inc, P/N 64040). These beads were used for calibration of the frequency/mass conversion and for flow stability control. Measurements were performed in 1 kHz and 2 kHz bandwidths.

D. DLS measurements

Solutions of monodisperse populations of particles were characterized by DLS, using a DynaPro Nanostar (Wyatt Technology Corp.). Fresh samples were prepared as described before, without the addition of reference particles, and measured in disposable plastic cuvettes. 15 μl of solution were used for each experiment. Each measurement consisted of 10 acquisitions of 10 s each, and signal analysis was performed directly by the acquisition instrument software (Dynamics, v. 7.1.5). The Rg (hydrodynamic radius) model was set to sphere, and water was selected as solvent. All measurements were performed at 25 °C.

E. Fit parameters estimation

For the analysis, each measurement trace is separated in two signals: the first containing only reference particle signatures and a second without visible particle signatures in the time-trace (here referred to as sample time-trace). To generate the reference particle trace, the reference signatures in the time-domain mass signal are extracted from the measurement trace and the baseline subtracted. The baseline is calculated by averaging 20 points before and after each particle signature. After removing the baseline, the reference signatures are autocorrelated and the curves summed. The resulting curve is fitted to estimate the flow velocity, using the particle size as known fit parameter.

To detect the buoyant mass and the size of the unknown particles, the sample time-trace is analyzed as follows: first, a high-pass filter (1 Hz cutoff frequency) is applied to remove the frequency baseline and the slow varying noise terms. Then, the stability of the flow during measurement is checked by comparing the autocorrelation functions of different portions of the trace. Once the stability of the flow is confirmed, the autocorrelation of the complete sample time-trace is calculated and fitted. Flow velocity, estimated from the added reference particles, is used as known parameter for the fitting, while curve amplitude and particle size are estimated from the fit. Eq. (12) is used as fit function, and the temporal evolution of the concentration fluctuations is calculated with Eq. (14).

The uncertainty on the estimated parameters is calculated using a bootstrap algorithm.[35] A pool of 500 pseudo time-traces is generated from which independent autocorrelation curves could be calculated. Because of the time correlation of the data of interest, the uncertainty estimation of the parameters is based on the Stationary Bootstrap method,[36] here described briefly: each pseudo time-trace is obtained by selecting random blocks of the original time-trace and combining them to generate a new trace, with a number of points equal or higher than the original trace. The number of observations per block is random and it is based on a geometric distribution, with average block length of $\sim$10 s, an interval much longer than the correlation time of the particles in the channel. The means of the obtained fit parameters are taken as best fit parameters, and their standard deviation as uncertainty of the estimation. All sample curves taken at different flow velocities are fitted using a single size parameter to monitor the goodness of the size estimation under different dispersion behaviors.

Experimental autocorrelations are calculated as follows:

$$\hat{C}[k] = \frac{1}{N-k}\sum_{i=1}^{N-k} \delta f_i \cdot \delta f_{i+k}, \tag{27}$$

where δf_i denotes the sampled and high-pass filtered signal ($i = 1 \ldots N$ and $N = [T_{meas} \cdot f_s]$, f_s sampling rate).

IV. MONTE CARLO SIMULATIONS

We tested our approximate solution for $\delta c_m(x,t)$ using MC simulations, to study dispersion under different flow velocities and to check the validity of the designed transition factor $A(t)$ (Eq. (26)). Since finite-size effects can mask the axial dispersion caused by particle diffusion and could also influence the transition between the advection and the Taylor regime, the simulations were performed in the limit of point-like particles. Therefore, MC simulations can be presented in terms of normalized time τ_D and distance χ, defined as

$$\chi = Dx/(U_{avg}a^2), \tag{28}$$

where as characteristic dimension we used the effective channel radius defined as $a = \sqrt{4bh/\pi^2}$. U_{avg} denotes the average velocity of the fluid and, in this case, it also

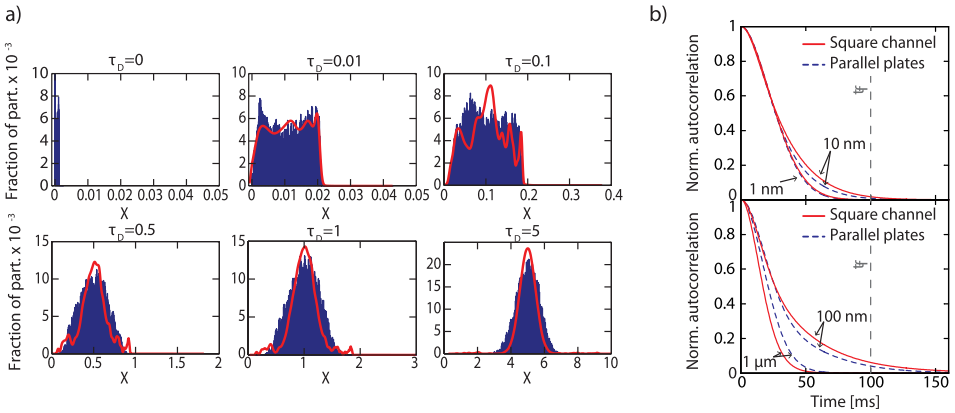

FIG. 3. (a) Monte Carlo simulation for a plug of 5000 pointlike particles. Because of the uniform probability of concentration fluctuation over the cross-section, the concentration fluctuations are approximated by a sheet of particles at $\tau = 0$ at the entrance of the channel. The histogram shows the numerical results, the red continuous line shows the expected curve, calculated with Eq. (14); (b) cross-section aspect ratio effects on autocorrelation signals from different size particles. The dashed vertical line represents the average time spent by the fluid in the embedded channel. The expected curves are generated for channels of square and parallel plate cross-sections, 3 μm high. The curves are calculated for finite-size particles.

coincides with the average velocity of the particles, as a consequence of the point-like assumption.

The MC simulation at different time points for a channel of aspect ratio $\beta = 3/8$, as the one employed for the mass measurements, is shown in Fig. 3(a). In terms of dimensional units, the simulation corresponds to following the dispersion of a plug of 50 nm particles in a $3 \times 8\ \mu m^2$ channel with an average flow velocity of $\approx$1.4 cm/s (Péclet number $\approx$ 400), a typical working condition for the SMR. As expected, precise matching between Eq. (14) and the simulation occurs only in the extreme cases of $\tau_D \ll 1$ and $\tau_D \gg 1$. However, the approximate solution developed here follows adequately the evolution of the sample plug, from the early convective regime to the final Gaussian distribution.

V. EFFECT OF CHANNEL ASPECT RATIO

By including finite-size corrections in the derived model, we generated expected autocorrelation curves for particles of different diameters flowing in rectangular microfluidic channels of arbitrary dimensions, to evaluate the influence of channel aspect ratio on the autocorrelation curve. The curves for two extreme cases, namely, a channel with square cross-section ($\beta = 1$) and a conduit formed by parallel plates ($\beta = 0$), are shown in Fig. 3(b). Square channels present the widest velocity distribution in the cross section, with maximum velocity being approximately twice the average flow velocity; on the contrary, parallel plate channels are characterized by a velocity profile extending from 0 to approximately 1.5 times the average flow velocity. Because of the wider velocity distribution, channels with $\beta \to 1$ present larger differences between autocorrelation curves for particles of different sizes and should be favored for size identification.

VI. RESULTS AND DISCUSSION

Nanoparticles of diameters ranging from a few to hundreds of nanometers were characterized by MCS to validate the ability of the analysis in detecting particle size using the developed dispersion model. A small concentration of 1.54 μm NIST polystyrene beads was added to each sample as calibration particles for the response of the resonator and for the detection of the flow velocity. As a consequence of their large mass ($\sim$100 fg), these particles are clearly visible in the time-domain mass signal and, with a size comparable to the channel cross-section, the particles present a very narrow velocity distribution, simplifying the detection of the flow velocity during measurement. Furthermore, as the buoyant mass of the particles is known, the induced frequency shifts also serve as calibration for the mass responsivity of the resonator ($\sim$20 mHz/fg). During data analysis, the reference particle signatures are separated from the time-domain mass trace, and their autocorrelation is fitted to obtain the average fluid velocity in order to compensate for small fluctuations in differential pressure or flow resistance. This information is then used during the analysis of the sample autocorrelation, leaving the curve amplitude and the particle size as free parameters of the fit curve (Fig. 4).

The analysis was tested on five different samples: 15 ± 1.5 nm (gold), 30 ± 3 nm (gold), 85 ± 6 nm (polystyrene), 210 ± 10 nm (polystyrene), and 490 ± 10 nm (polystyrene), as reported by the manufacturers. Each sample was measured under a variety of flow velocities to monitor particle dispersion at different time scales and increase the analysis resolution. The average residence time of the particles in the resonator ranged from $\sim$20 ms to $\sim$200 ms, and each mass trace was acquired for $\sim$30 s to a few minutes, the acquisition time being limited by the interaction of the particles with the channel walls, which leads to gradual clogging, and the stability of the flow velocity.

From the fit of the experimental autocorrelation curves, we estimated a size of 37 ± 1, 51 ± 2, 109 ± 24, 245 ± 40, and 537 ± 32 nm for the 15, 30, 93, 210, and 490 nm particles, respectively. The fit procedure and the behavior of the residuals with particle size are shown in Fig. 5. The uncertainties on the estimations of particle sizes are calculated with the bootstrap algorithm presented in Section III. Therefore, the uncertainty intervals take into account both the acquisition noise of the time-domain mass trace and flow instabilities, caused by pressure fluctuations or particle

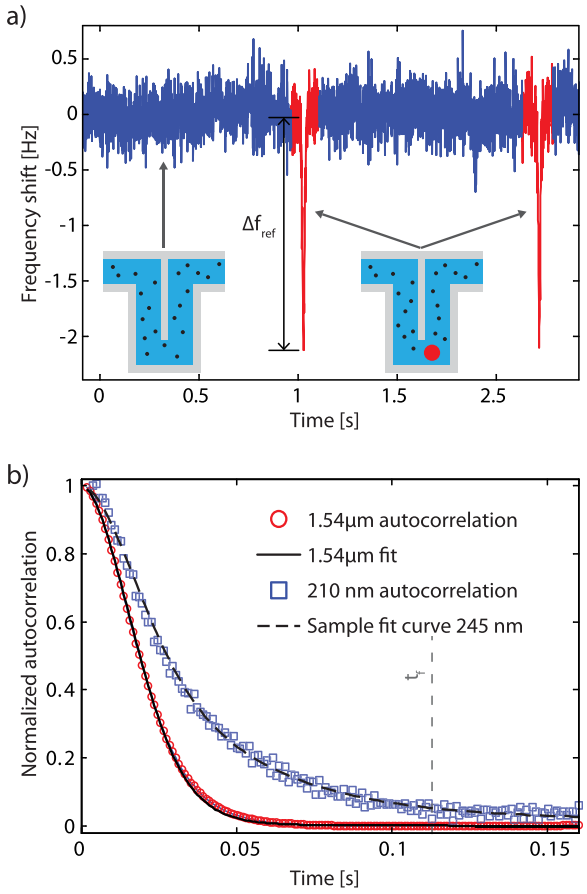

FIG. 4. (a) A short excerpt of the time-domain mass signal for a sample of 210 nm and 1.54 μm particles after high-pass filtering to remove baseline and low frequency noise terms. The large reference particles present clear signatures in the signal (in red). These signatures are removed from the time-trace and analyzed separately to calibrate the mass responsivity of the resonator and extract the flow parameters; (b) comparison between the autocorrelation of the 210 nm and 1.54 μm particles. Reference particles present a shorter correlation time, as larger particles move, on average, faster than the smaller particles. The solid black line shows the fit of the reference particle autocorrelation; the dashed black line shows the best fit curve, obtained for a sample of particles of 245 nm.

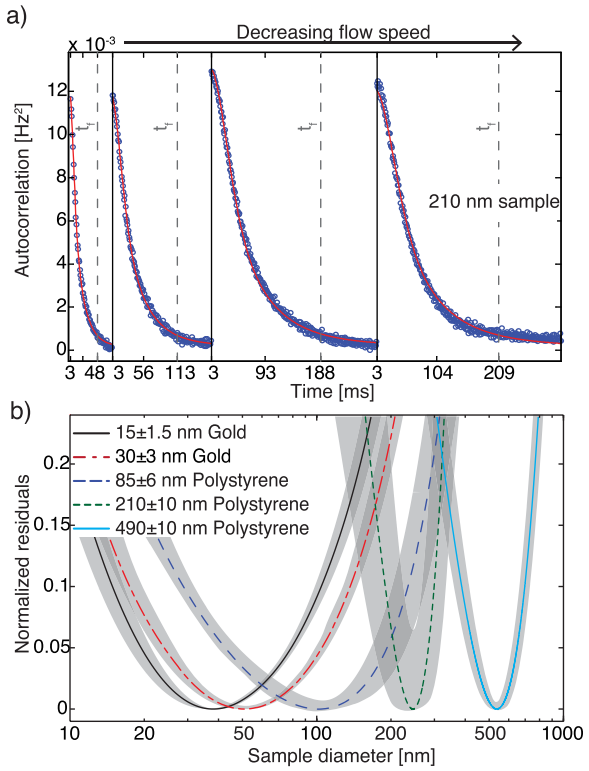

FIG. 5. (a) Autocorrelation curves obtained for the 210 nm particles at different flow velocities (blue). The particles are measured under different flow velocities to detect the dispersion at different regimes. The red line shows the fit curve, obtained for a particle diameter of 245 nm; (b) normalized residuals after fitting the experimental data with test autocorrelation curves of different diameters. The residuals were offset to their minimum residual value found, with 0 corresponding to the best fit obtained. The uncertainty intervals are calculated with the bootstrap method explained in Section III.

interactions with the walls, which might occur during the detection. The results obtained with our method present approximately a 25 nm overestimation of the particle sizes, possibly due to the approximation used in the model derivation and to tolerances in device dimensions. However, relative differences between particles can still be inferred from the analysis, showing that the samples under investigation ranged from few tens to hundreds of nanometers. The use of calibration particles for detecting the accuracy of the measurement could provide a solution for obtaining absolute size quantification during mass measurement. It is interesting to note that the MCS method applies for particles whose size is non-negligible with respect to the cross-section dimensions, as for the 490 nm particles, despite the simplistic approximations used for estimating the velocity distribution of finite-size particle. Under the experimental conditions, particles of these dimensions have very small diffusion lengths, and size characterization is mostly based on the quantification of the difference in average velocity between the sample and the reference particles. Furthermore, the largest relative uncertainty is obtained for the 85 nm polystyrene nanoparticles. The uncertainty value is not representative of the sample distribution, but depends on the measurement conditions. Particles of size ranging from ~50 to ~150 nm do not diffuse considerably during their transit time and present an average velocity almost coincident with the fluid velocity. In this regime, the identification of particle size cannot be based on sample diffusion, nor on average velocity, therefore resulting in a large size uncertainty. As expected, the relative uncertainty in the size measurement is different for the different particles. This is because sizing of all tested polystyrene particles relies mainly on their geometric exclusion from the walls, whereas the smaller gold particles are sized mainly based on their diffusivity.

The particles were also characterized by DLS, under similar conditions. The characterization returned values of 17.2 nm (Pd 26%), 37.6 nm (Pd 14%), 66 nm (Pd 19%), 248 nm (Pd 23%), and 473 nm (Pd 10%) for the 15, 30, 85, 210, and 490 nm particles, respectively. Pd denotes the percentage polydispersivity of the sample: for Pd $\leq$ 15%, the sample is considered monomodal and monodisperse; $15 < Pd \leq 30$ the sample is monomodal polydisperse, i.e., the population is monodisperse, but it presents a large distribution; higher Pd values correspond to heterogeneous populations.[37] High values of polydispersivity, likely corresponding to the presence of small aggregates of particles in solution,

might be the cause of the relatively large uncertainties obtained in size determination with the MCS analysis. However, no direct correspondence between MCS and sample distribution can currently be inferred.

The amplitude of the correlation function contains information on the mass and concentration of the particles in solution.[21] The curve amplitude is unrelated to its shape and, as a consequence, the MCS analysis allows independent and simultaneous measurement of mass and size of the particles (Fig. 6). As the sample concentration is known, the average buoyant mass of the particles can be calculated from Eq. (6) as

$$\Delta m_p = \sqrt{\frac{5C(0)}{c_0 V}} \cdot \left(\frac{\partial f}{\partial m}\right)^{-1}, \tag{29}$$

where $C(0)$ is the correlation amplitude at lag zero, c_0 is the particle concentration, V denotes the channel volume, and $f_{p0} = \Delta m_p \cdot (\partial f/\partial m)$ (with $\partial f/\partial m$ denoting the frequency/mass responsivity of the device). The definition given in Eq. (29) is strictly valid only for a sample of identical particles. The buoyant mass estimated from the MCS curve actually corresponds to $\sqrt{\langle \Delta m_p^2 \rangle}$ and it follows that, when dealing with samples presenting a large distribution of sizes, the estimated mass might be considerably different from the arithmetic mean mass.

The estimated values of buoyant mass are 32 ± 3 ag, 184 ± 17 ag, 26 ± 2 ag, 0.43 ± 0.05 fg, and 3.5 ± 0.3 fg for the 15, 30, 85, 210, and 490 nm particles, respectively. The uncertainty intervals reported include both the statistical error on the fitting of the correlation curves and the experimental uncertainty on the mass/frequency conversion. Systematic errors, due to device tolerances or sample preparation, are not included. As a comparison, the detection limit for single-particle measurements with these devices corresponds to ~30 fg, considering a minimum signal-to-noise ratio of 3, a detection limit more than three orders of magnitudes higher than the mass of the 85 nm particles.

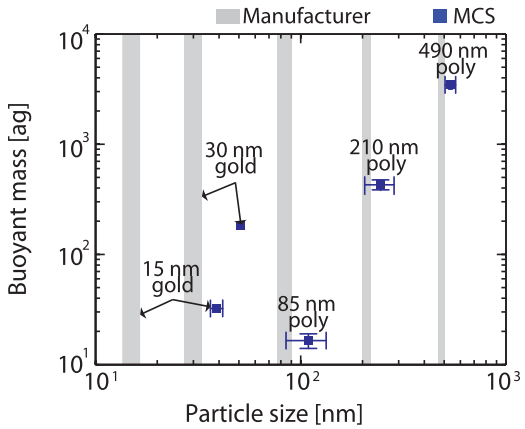

FIG. 6. Buoyant mass and size of the particles measured by MCS. The manufacturer specifications are reported for comparison. Size estimations with the MCS method show a deviation of approximately 25 nm from the manufacturer reported values; however, relative size differences between particles can be detected by the analysis. The non monotonic behavior of the mass with particle size clearly shows that the samples under examination were composed of different materials, with a large difference in density.

Although the absolute quantification of particle density is affected by the accuracy of the measurement, the non-monotonic variation of mass with particle sizes clearly indicates that the samples are composed of materials with a large density difference. The particle densities calculated from the size and mass estimations are 2.04 ± 0.30 g/cm^3, 3.65 ± 0.56 g/cm^3, 1.02 ± 0.02 g/cm^3, 1.06 ± 0.03 g/cm^3, and 1.04 ± 0.01 g/cm^3 for the 15, 30, 85, 210, and 490 nm samples, respectively. As expected, the gold particles are strongly affected by the accuracy of the measurement and present a much lower value compared to the theoretical density of bulk gold of 19.3 g/cm^3; in contrast, a minor deviation is obtained for the larger polystyrene particles, whose estimated densities present good agreement with the expected density of polystyrene of 1.05–1.06 g/cm^3.

SMRs have already been used for density measurements by detecting the variation of buoyant mass when measuring the same sample in solutions of different densities.[19,38,39] Although this method can achieve very high resolution, an implicit assumption is that the particles do not undergo any change when suspended in different solutions, a condition that cannot always be met. Furthermore, density measurements of particles composed of heavy materials, such as gold nanoparticles, would be equally challenging when performed by density buffer variation: for the method to be efficient, the interval of solution densities used for the characterization should approach, or contain, the density of the sample of interest.

Finally, we present a set of measurements performed on a sample with a bimodal distribution of particles, namely, 93 nm and 490 nm polystyrene particles. Figure 7 shows the experimental correlation curves measured with different flow velocities. The curves are compared to the fit functions obtained by considering the sample composed of only one of the two populations of nanoparticles or by both populations. The single-population curves cannot describe the correlation function of the mass signal at all dispersion times; on the contrary, the functions calculated considering a bimodal distribution better follows the behavior of the curves at all times, showing that information on sample composition is contained in the correlation shape. We used a least-square approach to find the superposition of the autocorrelation curves of the two populations which best fits the experimental correlation curves at the different flow velocities. Similarly to size estimation, the amplitude of the fit function was free to vary between measurements, while a single value of the ratio between the two populations was used to fit all curves. The confidence interval on the estimation parameter was obtained using a bootstrap algorithm, as explained before. We found that the 93 nm sample accounts for $(37 \pm 5)\%$ of the autocorrelation signal. Knowing the total dissolved mass (2.5 mg/ml) and assuming that the particles have equal densities, we calculated a concentration of $(5.6 \pm 0.1) \times 10^{12}$ ml^{-1} and $(4.1 \pm 0.9) \times 10^{8}$ ml^{-1} for the 93 nm and for the 490 nm nanoparticles, respectively. Their estimated density is 1.07 ± 0.01 g/cm^3. As for the previous measurements, the calculated intervals only include the statistical errors of the fit parameters caused by the acquisition noise and flow instabilities. Systematic errors, such as during

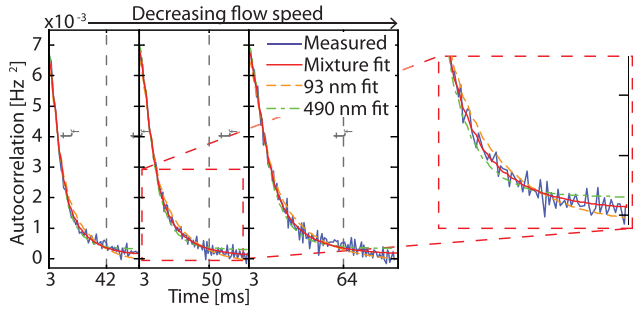

FIG. 7. Autocorrelation curves of a mixed sample composed of 93 nm and 490 nm beads (manufacturer values). The figure shows the fits obtained when considering a sample composed of a monodisperse (dashed lines) or a bimodal (solid red curve) distribution. The monodisperse curves cannot fit properly the experimental autocorrelation curves acquired at different flow velocities, showing that the heterogeneity of the sample can be inferred from the MCS signal.

sample preparation or the systematic bias in particle size determination, can account for the differences between the expected and measured values. Although the measurement demonstrates that the autocorrelation shape can be an indicator of the polydispersivity of the particle population, quantification of the properties of polydisperse samples can be challenging when no prior knowledge is available.

VII. CONCLUSIONS

We have introduced here a method of nanoparticle characterization by suspended microchannel resonators, which allows the simultaneous measurement of size and mass of particles in solution. Importantly, the method can be used even when the particles are much lighter than the single-particle detection limit. To do so, we designed an approximate solution for the calculation of the axial dispersion of particles while subjected to a laminar flow in a rectangular cross-section channel, and we integrated this solution into the description of the correlation curve of the time-domain mass signal.

The solution developed here applies to particles of finite size, even in the limit of particle diameter comparable to the channel dimensions, and is valid in a large range of dispersion regimes, from the early advection dominated regime to the final Taylor-Aris regime.

Both numerical and experimental results have been shown to confirm the predictions of our analysis. Monte Carlo simulations were used to validate the model behavior under different working conditions, in terms of cross-section aspect ratio and particle diffusivity. Experimental results on particles of different sizes and materials have also been presented, showing that the analysis can correctly detect the dimension range of the particles under examination. The measurements show an accuracy of few tens of nanometers in the absolute estimation of particle sizes. This is likely caused by the simplified model used for describing the particle behavior in the channel and by tolerances in the device dimensions. Calibration of the device response and the combined use of resonators with different microfluidic channels might produce size estimates with higher accuracy and increase the application range of the analysis. Nevertheless, the measurements presented here show that SMR devices can provide simultaneous detection of mass, density, and particle size in the sub-micrometer regime. Furthermore, despite the low diffusivity of micrometer-size particles, differences in average velocity might enable characterization even in the limit of non-diffusing objects, provided that the channel dimensions are comparable to the particles under examination.

Additionally, we presented a measurement on a sample composed of two types of particles of known diameter. We showed that information on the sample distribution can be recovered from the autocorrelation shape, although the analysis of a completely unknown sample might present several technical difficulties. We expect that already existing algorithms for extracting polydispersivity information by analogous correlation techniques[40,41] could be adapted to our analysis and enable the detection of size distribution of mono- and polydisperse samples by Mass Correlation Spectroscopy.

Furthermore, we think that the model developed here could find broader applications in microfluidics, other than that of mass measurements by resonator devices. The rapid calculation of the axial dispersion of a sample of particles in microfluidic channels might help in the design of reactors and mixing devices, where information on the residence time distribution of the sample in the channel is of fundamental importance.

Finally, our model could also be applied to other type of correlation analysis usually performed on static samples. We envision that Dynamic Light Scattering and Fluorescence Correlation Spectroscopy could benefit from the description of particle dispersion, enabling simple application of these techniques to samples subjected to laminar flows in microfluidic channels. Light intensity or fluorescence fluctuations due to particle number variation flowing through the illuminated volume could be analyzed in terms of axial dispersion and average velocity of the particles, as presented here for mass measurements. This could potentially extend the range of applications of such techniques to sub-micrometer/micrometer size particles undergoing structural changes while traveling in microfluidic reactors.

ACKNOWLEDGMENTS

Suspended Microchannel Resonator devices were generously provided by the laboratory of Professor Scott Manalis (MIT, Cambridge, MA). This work was funded by the Göttingen Graduate School for Neurosciences, Biophysics, and Molecular Biosciences, the Max Planck Society, and the Max Planck Institute for Biophysical Chemistry.

[1]R. Pecora, *Dynamic Light Scattering: Applications of Photon Correlation Spectroscopy* (Springer Science & Business Media, 1985).
[2]M. S. Bello, R. Rezzonico, and P. G. Righetti, "Use of Taylor-Aris dispersion for measurement of a solute diffusion coefficient in thin capillaries," Science (New York, N.Y.) **266**, 773–776 (1994).
[3]T. M. Laue, "Analytical ultracentrifugation," in *Current Protocols in Protein Science* (John Wiley & Sons, Inc., 2001).

[4]J. Zhu, S. K. Ozdemir, Y.-F. Xiao, L. Li, L. He, D.-R. Chen, and L. Yang, "On-chip single nanoparticle detection and sizing by mode splitting in an ultrahigh-Q microresonator," Nat. Photonics **4**, 46–49 (2010).
[5]T. K. Das, "Protein particulate detection issues in biotherapeutics development current status," AAPS PharmSciTech **13**, 732–746 (2012).
[6]W. Anderson, D. Kozak, V. A. Coleman, S. K. Jmting, and M. Trau, "A comparative study of submicron particle sizing platforms: Accuracy, precision and resolution analysis of polydisperse particle size distributions," J. Colloid Interface Sci. **405**, 322–330 (2013).
[7]W. Cheng, X.-F. Zhou, and R. G. Compton, "Electrochemical sizing of organic nanoparticles," Angew. Chem. **125**, 13218–13220 (2013).
[8]P. Linkov, M. Artemyev, A. E. Efimov, and I. Nabiev, "Comparative advantages and limitations of the basic metrology methods applied to the characterization of nanomaterials," Nanoscale **5**, 8781–8798 (2013).
[9]J. C. H. Spence, *High-Resolution Electron Microscopy* (Oxford University Press, 2008).
[10]S. E. McNeil, "Size measurement of nanoparticles using atomic force microscopy—Springer," in *Characterization of Nanoparticles Intended for Drug Delivery* (Humana Press, 2011).
[11]A. K. Naik, M. S. Hanay, W. K. Hiebert, X. L. Feng, and M. L. Roukes, "Towards single-molecule nanomechanical mass spectrometry," Nat. Nanotechnol. **4**, 445–450 (2009).
[12]M. S. Hanay, S. Kelber, A. K. Naik, D. Chi, S. Hentz, E. C. Bullard, E. Colinet, L. Duraffourg, and M. L. Roukes, "Single-protein nanomechanical mass spectrometry in real time," Nat. Nanotechnol. **7**, 602–608 (2012).
[13]J. Tamayo, P. M. Kosaka, J. J. Ruz, A. San Paulo, and M. Calleja, "Biosensors based on nanomechanical systems," Chem. Soc. Rev. **42**, 1287–1311 (2013).
[14]K. Jensen, K. Kim, and A. Zettl, "An atomic-resolution nanomechanical mass sensor," Nat. Nanotechnol. **3**, 533–537 (2008).
[15]J. Chaste, A. Eichler, J. Moser, G. Ceballos, R. Rurali, and A. Bachtold, "A nanomechanical mass sensor with yoctogram resolution," Nat. Nanotechnol. **7**, 301–304 (2012).
[16]T. P. Burg, M. Godin, S. M. Knudsen, W. Shen, G. Carlson, J. S. Foster, K. Babcock, and S. R. Manalis, "Weighing of biomolecules, single cells and single nanoparticles in fluid," Nature **446**, 1066–1069 (2007).
[17]R. A. Barton, B. Ilic, S. S. Verbridge, B. R. Cipriany, J. M. Parpia, and H. G. Craighead, "Fabrication of a nanomechanical mass sensor containing a nanofluidic channel," Nano Lett. **10**, 2058–2063 (2010).
[18]P. Waggoner, C. Tan, and H. Craighead, "Microfluidic integration of nanomechanical resonators for protein analysis in serum," Sens. Actuators, B **150**, 550–555 (2010).
[19]W. H. Grover, A. K. Bryan, M. Diez-Silva, S. Suresh, J. M. Higgins, and S. R. Manalis, "Measuring single-cell density," Proc. Natl. Acad. Sci. **108**, 10992 (2011).
[20]S. Olcum, N. Cermak, S. C. Wasserman, K. S. Christine, H. Atsumi, K. R. Payer, W. Shen, J. Lee, A. M. Belcher, S. N. Bhatia, and S. R. Manalis, "Weighing nanoparticles in solution at the attogram scale," Proc. Natl. Acad. Sci. **111**, 1310 (2014).
[21]M. M. Modena, Y. Wang, D. Riedel, and T. P. Burg, "Resolution enhancement of suspended microchannel resonators for weighing of biomolecular complexes in solution," Lab Chip **14**, 342–350 (2014).
[22]S. Dohn, W. Svendsen, A. Boisen, and O. Hansen, "Mass and position determination of attached particles on cantilever based mass sensors," Rev. Sci. Instrum. **78**, 103303 (2007).
[23]In statistics, Eq. (4) is called autocovariance; however, in other fields, it is often defined as autocorrelation. Here, we will use this second convention.
[24]M. Doshi, P. Daiya, and W. Gill, "Three dimensional laminar dispersion in open and closed rectangular conduits," Chem. Eng. Sci. **33**, 795–804 (1978).
[25]K. Ekambara and J. B. Joshi, "Axial mixing in laminar pipe flows," Chem. Eng. Sci. **59**, 3929–3944 (2004).
[26]G. Taylor, "Dispersion of soluble matter in solvent flowing slowly through a tube," Proc. R. Soc. London, Ser. A **219**, 186–203 (1953).
[27]O. Levenspiel, *Tracer Technology: Modeling the Flow of Fluids* (Springer, 2011).
[28]R. Aris, "On the dispersion of a solute in a fluid flowing through a tube," Proc. R. Soc. London, Ser. A **235**, 67–77 (1956).
[29]D. Dutta, A. Ramachandran, and D. T. Leighton, Jr., "Effect of channel geometry on solute dispersion in pressure-driven microfluidic systems," Microfluid. Nanofluid. **2**, 275–290 (2006).
[30]S. C. James and C. V. Chrysikopoulos, "Effective velocity and effective dispersion coefficient for finite-sized particles flowing in a uniform fracture," J. Colloid Interface Sci. **263**, 288–295 (2003).
[31]I. C. Christov and H. A. Stone, "Shear dispersion in dense granular flows," Granular Matter **16**, 509–515 (2014).
[32]S. Haber and R. Mauri, "Lagrangian approach to time-dependent laminar dispersion in rectangular conduits. Part 1. Two-dimensional flows," J. Fluid Mech. **190**, 201–215 (1988).
[33]T. P. Burg, J. E. Sader, and S. R. Manalis, "Nonmonotonic energy dissipation in microfluidic resonators," Phys. Rev. Lett. **102**, 228103 (2009).
[34]T. Burg, A. Mirza, N. Milovic, C. Tsau, G. Popescu, J. Foster, and S. Manalis, "Vacuum-packaged suspended microchannel resonant mass sensor for biomolecular detection," J. Microelectromech. Syst. **15**, 1466–1476 (2006).
[35]B. Efron and R. J. Tibshirani, *An Introduction to the Bootstrap* (Chapman & Hall, 1994).
[36]D. N. Politis and J. P. Romano, "The stationary bootstrap," J. Am. Stat. Assoc. **89**, 1303–1313 (1994).
[37]Wyatt Technology Corporation, "DYNAMICS User's guide, M1400 Rev. I" (2010).
[38]S. Son, A. Tzur, Y. Weng, P. Jorgensen, J. Kim, M. W. Kirschner, and S. R. Manalis, "Direct observation of mammalian cell growth and size regulation," Nat. Methods **9**, 910 (2012).
[39]A. K. Bryan, V. C. Hecht, W. Shen, K. Payer, W. H. Grover, and S. R. Manalis, "Measuring single cell mass, volume, and density with dual suspended microchannel resonators," Lab Chip **14**, 569 (2014).
[40]S. W. Provencher, "A constrained regularization method for inverting data represented by linear algebraic or integral equations," Comput. Phys. Commun. **27**, 213–227 (1982).
[41]D. E. Koppel, "Analysis of macromolecular polydispersity in intensity correlation spectroscopy: The method of cumulants," J. Chem. Phys. **57**, 4814–4820 (1972).